



Quantum Hall effect of Weyl fermions in n-type semiconducting tellurene

Gang Qiu^{1,2}, Chang Niu^{1,2}, Yixiu Wang³, Mengwei Si^{1,2}, Zhuocheng Zhang^{1,2}, Wenzhuo Wu³ and Peide D. Ye^{1,2}✉

Dirac and Weyl nodal materials can host low-energy relativistic quasiparticles. Under strong magnetic fields, the topological properties of Dirac/Weyl materials can directly be observed through quantum Hall states. However, most Dirac/Weyl nodes generically exist in semimetals without exploitable band gaps due to their accidental band-crossing origin. Here, we report the first experimental observation of Weyl fermions in a semiconductor. Tellurene, the two-dimensional form of tellurium, possesses a chiral crystal structure which induces unconventional Weyl nodes with a hedgehog-like radial spin texture near the conduction band edge. We synthesize high-quality n-type tellurene by a hydrothermal method with subsequent dielectric doping and detect a topologically non-trivial π Berry phase in quantum Hall sequences. Our work expands the spectrum of Weyl matter into semiconductors and offers a new platform to design novel quantum devices by marrying the advantages of topological materials to versatile semiconductors.

The emergence of graphene¹ has triggered vast interest in studying the properties of relativistic particles in low energy spectra of topological materials. For example, under high magnetic fields, the unconventional sequence of graphene quantum Hall states at filling factor $\nu = 4(n + \frac{1}{2})$ (here $n = 0, 1, 2, \dots$) suggests the presence of Dirac fermions with π Berry phase^{2,3}, which reflects the topological nature of Dirac points. Since then, many other classes of topological materials with Dirac/Weyl nodal features in their band structures have been predicted and identified^{4,5} with great potential for spintronics, optoelectronics and quantum computing applications. However, these Dirac/Weyl points generated by the crossing of either two bands or two branches of spin polarized bands are generically limited to semimetals without exploitable band gaps. In this work we introduce a new semiconductor system: tellurene (two-dimensional (2D) form of tellurium) with Weyl nodal features in the vicinity of conduction band minima. The combination of topological materials and semiconductors in the two-dimensional limit allows us to explore the Weyl physics in a more controllable manner and to design topological devices.

Weyl nodes in chiral tellurene and n-type atomic layer deposition (ALD) doping

Trigonal tellurium (Te) is a narrow band gap semiconductor with a unique one-dimensional helical atomic structure. The crystal consists of three-fold screw-symmetric atomic chains interconnected by van der Waals forces, as shown in Fig. 1a. The screw symmetry distinguishes two irreducible enantiomers with opposite chirality in real space, which fall into either the $P3_21$ or the $P3_121$ space group, depending on the handedness. One prominent feature of the band structure occurs at the bottom of the conduction band at the H point (Fig. 1b,c), where the spin degeneracy is lifted to form band crossing due to strong spin-orbit coupling (SOC) and broken inversion symmetry. Despite the similarity to the energy dispersion of a conventional Rashba band, Te exhibits a hedgehog-like radial spin texture with positive (negative) monopole charge in momentum space arising from the topologically non-trivial Weyl nodes^{6–10},

which is fundamentally distinct from tangential spin texture of Rashba bands⁶ (as we shall further discuss later). The existence of Weyl points in Te has been predicted recently^{6–8,10}, with topological properties in accordance with the framework of newly proposed Kramers–Weyl nodes in chiral crystals with strong SOC¹¹. In chiral crystal systems like CoSi and Ag₃Se, angle-resolved photoemission spectroscopy^{12,13} and magneto-transport¹⁴ provide evidence for Kramers–Weyl fermions. Note that in Te, since the H point is not a time reversal invariant momentum point, the degeneracy is not protected by Kramers theorem (which is the prerequisite of Kramers–Weyl nodes), but is instead guaranteed by its three-fold rotational symmetry. Nonetheless, despite the different mechanism leading to Weyl nodes, they both share similarity in band topology, spin textures and other topological properties.

To date, most magneto-transport measurements have been performed on bulk Te samples^{15–17}, where the resolution of Shubnikov–de Haas (SdH) oscillation features was limited by the sample quality as well as weak 2D Landau quantization. A recently developed hydrothermal growth method yields atomically flat 2D Te films with surfaces free of dangling bonds^{18–20} (Fig. 1e inset), whose thickness ranges from a couple of atomic layers to tens of nanometres. These 2D Te films are coined as tellurene in analogy to other 2D elemental materials such as graphene, stanene and phosphorene. Much better developed SdH oscillations as well as quantum Hall states were observed in these p-type tellurene films²¹, adding a new member into the scarce family of high-mobility 2D materials hosting the quantum Hall effect which includes graphene^{2,3,22}, black phosphorus^{23–25}, InSe²⁶ and some transition metal dichalcogenides^{27–30}. However, due to the unintentional p-type doping in Te, the chemical potential is usually pinned near the valence band edge. Therefore, so far most of the experiments have been limited to holes and little about the properties of the conduction band is shown by transport measurements^{19,21,31}. Here, we successfully converted tellurene films into n-type using an atomic layer deposition (ALD) dielectric doping technique without degrading electron mobility^{32,33}, which grants us access to the conduction band to explore

¹School of Electrical and Computer Engineering, Purdue University, West Lafayette, IN, USA. ²Birck Nanotechnology Centre, Purdue University, West Lafayette, IN, USA. ³School of Industrial Engineering, Purdue University, West Lafayette, IN, USA. ✉e-mail: yep@purdue.edu

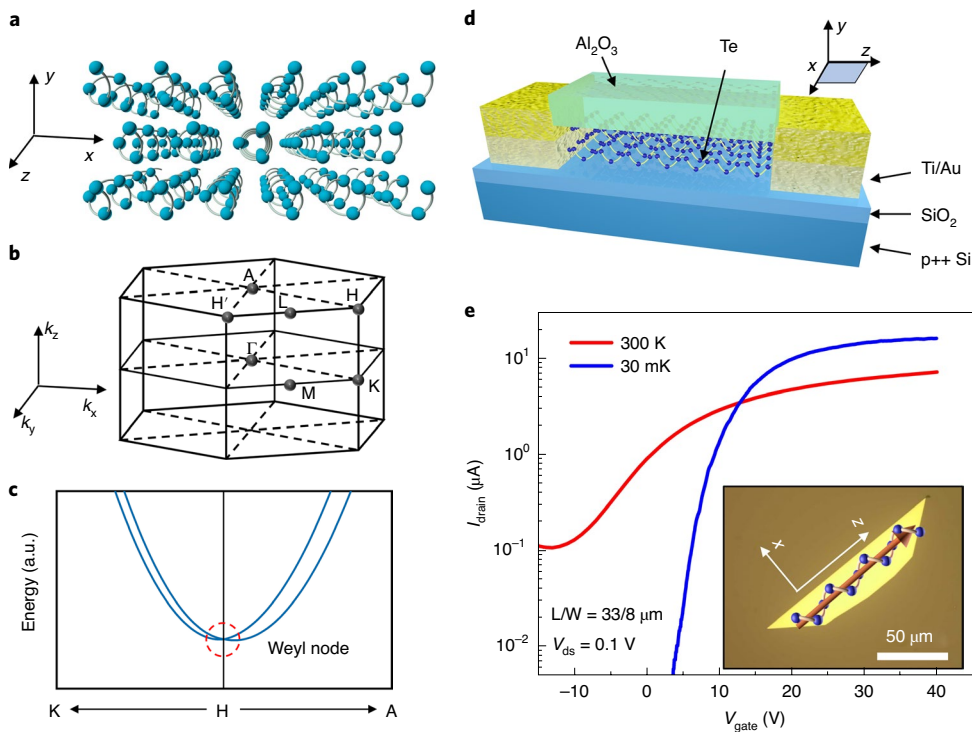


Fig. 1 | Crystal structure of Te and n-type ALD doped tellurene devices. **a**, Crystal structure of Te with helical atomic chains. **b**, First Brillouin zone of Te. The conduction band minima are located at the corner points H and H'. **c**, Zoomed-in energy dispersion of lowest spin-split bands along K-H-A line. A Weyl node is formed at the H point, as highlighted by the red dashed circle. a.u., arbitrary units. **d**, Schematic view of an n-type Te device with a global back gate and ALD doping layer on top. **e**, $I_{\text{drain}} - V_{\text{gate}}$ transfer curves of a typical ALD doped n-type device with aspect ratio $L/W = 33 \mu\text{m}/8 \mu\text{m}$ measured at room temperature (red) and cryostat temperature (blue) with two-terminal configuration under drain bias $V_{\text{ds}} = 0.1 \text{ V}$. Inset: an optical image of an as-synthesized tellurene film obtained from hydrothermal growth method. The helical chains (z axis) are aligned along the longer edge of the film, as indicated by the red arrow. All the Hall bar devices are also fabricated along the z axis.

more exotic physics of Weyl fermions through quantum Hall states. A schematic diagram of an n-type doped device is illustrated in Fig. 1d. The as-synthesized tellurene films were dispersed onto a degenerately doped silicon substrate with a 90 nm SiO_2 insulating layer on top, followed by patterning and deposition of titanium/gold (Ti/Au) metal contacts. We chose low work function metal contacts (Ti) to lower the electron Schottky barrier height and accommodate n-type transport. A layer of alumina was subsequently deposited onto tellurene film by ALD grown at 200 °C, converting the tellurene film from p-type to n-type, as confirmed by transfer curves (drain current I_{drain} versus gate voltage V_{gate}) of a tellurene field-effect transistor at both room temperature and cryogenic temperature (see Fig. 1e). A similar ALD doping method has also been reported on other material systems like black phosphorus^{34–36} and silicon³⁷. The doping mechanism is commonly attributed to the threshold voltage shift caused by positive fixed charges in low-temperature ALD-grown films³⁴ or the interface electric dipole field³⁷.

Quantum Hall effect in tellurene wide quantum well

For magneto-transport measurements, six-terminal Hall bar devices were fabricated as shown in Fig. 2a (see Methods for more fabrication and measurement details). We investigated over 20 devices with typical film thickness ranging from 10 to 20 nm and all of them exhibited similar and reproducible behaviour. Here, all the data presented are from one 12-nm-thick high-quality device, unless otherwise specified (additional data sets from other devices are available in Extended Data Fig. 1 and Supplementary Note 1). The global back gate allows us to tune the 2D electron density from 2×10^{12} to $1 \times 10^{13} \text{ cm}^{-2}$. Representative longitudinal (R_{xx}) and transverse (R_{xy}) magnetoresistance curves measured at gate voltage $V_g = 10 \text{ V}$

are plotted in Fig. 2b, with a Hall density n of $2.5 \times 10^{12} \text{ cm}^{-2}$ and a Hall mobility μ of $6,000 \text{ cm}^2 \text{ V}^{-1} \text{ s}^{-1}$. The onset of SdH oscillations is around 2 T, leading to an estimated quantum mobility of $5,000 \text{ cm}^2 \text{ V}^{-1} \text{ s}^{-1}$, which is close to Hall mobility within a reasonable margin. At a B field of around 24 T and 32 T, R_{xy} is fully quantized into an integer fraction of h/e^2 (corresponding to filling factor $\nu = 3$ and 4), and R_{xx} also drops to 0, a hallmark of the quantum Hall effect³⁸. As shown in Fig. 2c, by fixing the B field at 42 T and sweeping the back gate voltage, all filling factors from 2–8 are resolved (although not all fully quantized due to Landau level broadening), suggesting all the degeneracies, including spin and valley, have been lifted. By mapping out R_{xx} through the $V_g - B$ parameter space, we can construct the Landau fan diagram in a colour map as in Fig. 2d. Since the conduction band edge is located at two inequivalent H (H') points in the first Brillouin zone accounting for two-fold valley degeneracy, it is conceivable that each Landau level consists of four degenerate energy states (two for valley degeneracy g_v and two for spin degeneracy g_s) like graphene, with cyclotron energy gap

$$E_c = \hbar \omega_c = \frac{\hbar e B}{m^*} \quad (1)$$

at filling factors of 4, 8, 12 and so on. Here, \hbar is the reduced Planck constant, e is the electron charge and m^* is the effective mass. Following this argument, we should expect that by sweeping towards higher B field the energy gap should increase monotonically as the Fermi level approaches lower filling factors in the sequence of $4n$ (that is, 12, 8, 4, and so on), since the cyclotron energy $\frac{\hbar e B}{m^*}$ increases linearly with the magnetic field. Yet, we notice from Fig. 2b that the gap at $\nu = 12$ is significantly larger than that at $\nu = 8$, suggesting the

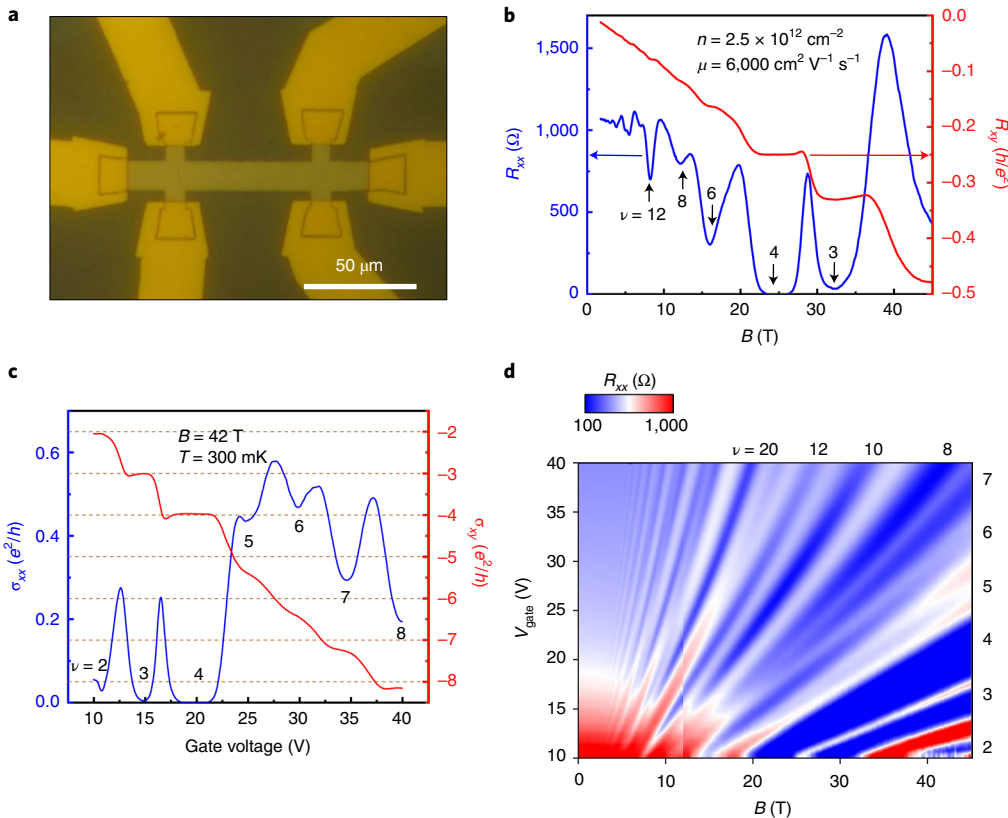


Fig. 2 | Quantum Hall effect in tellurium 2D electron gas. **a**, An optical image of a six-terminal Hall bar device. **b**, Longitudinal (R_{xx} in blue) and transverse (R_{xy} in red) resistance as a function of magnetic field. The extracted Hall density n and Hall mobility μ are $2.5 \times 10^{12} \text{ cm}^{-2}$ and $6,000 \text{ cm}^2 \text{ V}^{-1} \text{ s}^{-1}$, respectively. **c**, σ_{xx} and σ_{xy} as a function of back gate voltage. The gate oxide is 90 nm SiO₂. **d**, Colour mapping of R_{xx} by sweeping both back gate voltage and magnetic field. The data from 0–12 T and 12–45 T are measured from the same device in a superconducting magnetic system at 30 mK and a hybrid magnetic system at 300 mK, respectively.

simple four-level single particle picture cannot explain these unconventional sequences.

To understand this anomaly, we first focus on SdH oscillation features in the relatively low B field regime. The blue curve of Fig. 3a shows the normalized longitudinal resistance R_{xx} versus magnetic field (0–12 T) in another high mobility sample. Besides the predominant set of oscillations (marked by black arrows), a secondary set of weaker oscillations is also resolved (grey arrows). Due to the low oscillation frequency and limited observation window, it is difficult to disentangle two sets of oscillations by simply performing fast Fourier transform. Hence, we use the complete Lifshitz-Kosevich (L-K) formula to fit the SdH experimental data and distinguish two sets of oscillation features. The superposition of two sets of SdH oscillations in single electron picture can be described by

$$\frac{\Delta R_{xx}}{R_{xx}} = \sum_{D=1,2} \sum_{r=1}^{N_r} \frac{r\lambda}{\sinh(r\lambda)} \exp\left(\frac{-r\pi m^*}{\tau_D eB}\right) \cos\left(r\left(2\pi \frac{B_{f,D}}{B} - \pi + \varphi_D\right)\right) \quad (2)$$

Here, the first sum over D refers to two sets of oscillations and higher order harmonics up to $N_r = 20$ were taken into account in our fitting. The thermal damping term is $\lambda = 2\pi^2 m^* k_B T / \hbar eB$. We also parameterized the carrier lifetime τ_D , oscillation frequency $B_{f,D}$ and phase offset φ_D for both sets. The resistance minima are evenly spaced in the $1/B$ plot, hence the period in $1/B$ can be translated into SdH oscillation frequency $B_f = \frac{1}{\Delta(1/B)}$. The best fitting results (red curve in Fig. 3a) yield a dominant set of oscillations with frequency $B_{f,1} = 38.9 \text{ T}$, carrier lifetime $\tau_1 = 0.28 \text{ ps}$ and phase offset

$\varphi_1 = 0.97\pi$. The secondary set of oscillations were also well captured with frequency $B_{f,2} = 35.8 \text{ T}$, carrier lifetime $\tau_2 = 0.20 \text{ ps}$ and phase offset $\varphi_2 = 1.15\pi$. We conjecture that two sets of independent oscillations arise from the unique ALD doping scheme of the n-type Te films. The fixed positive charges in the ALD dielectrics will attract a layer of electrons on the top surface with relatively lower carrier mobility (and shorter lifetime) due to low interface quality and the back gate will induce another layer of charge on the bottom surface, as indicated in Fig. 3b. Following the same L-K formula, we can extend our simulation of SdH oscillations to the entire V_g - B parameter space by assuming that the oscillation frequency for each set has a linear dependence on the back-gate bias and meanwhile we set both phase shifts to π , which we shall further validate later. We intentionally exaggerated the carrier mobility in Fig. 3e in order to highlight the Landau levels. Our calculation (Fig. 3e) successfully reproduced the major features in the experiment (Fig. 3d). The oscillation frequency of the predominant (bottom layer) set increases from 17.9 T to 57.8 T as the back-gate sweeps from 10 V to 40 V , whereas the weaker set (top layer) increases from 21.7 T to 46.5 T . This is consistent with our dual-layer assumption as the frequency of the predominant set associated with the bottom layer is more sensitive to the back-gate modulation as illustrated in Fig. 3c, whereas the top layer with lower mobility is less sensitive since the gate-induced electric field is partially screened out by the bottom layer of electrons.

Topologically non-trivial π Berry phase

The most significant feature from the mapping in Fig. 3d,e is that the V_g - B parameter space can only be accurately reproduced when

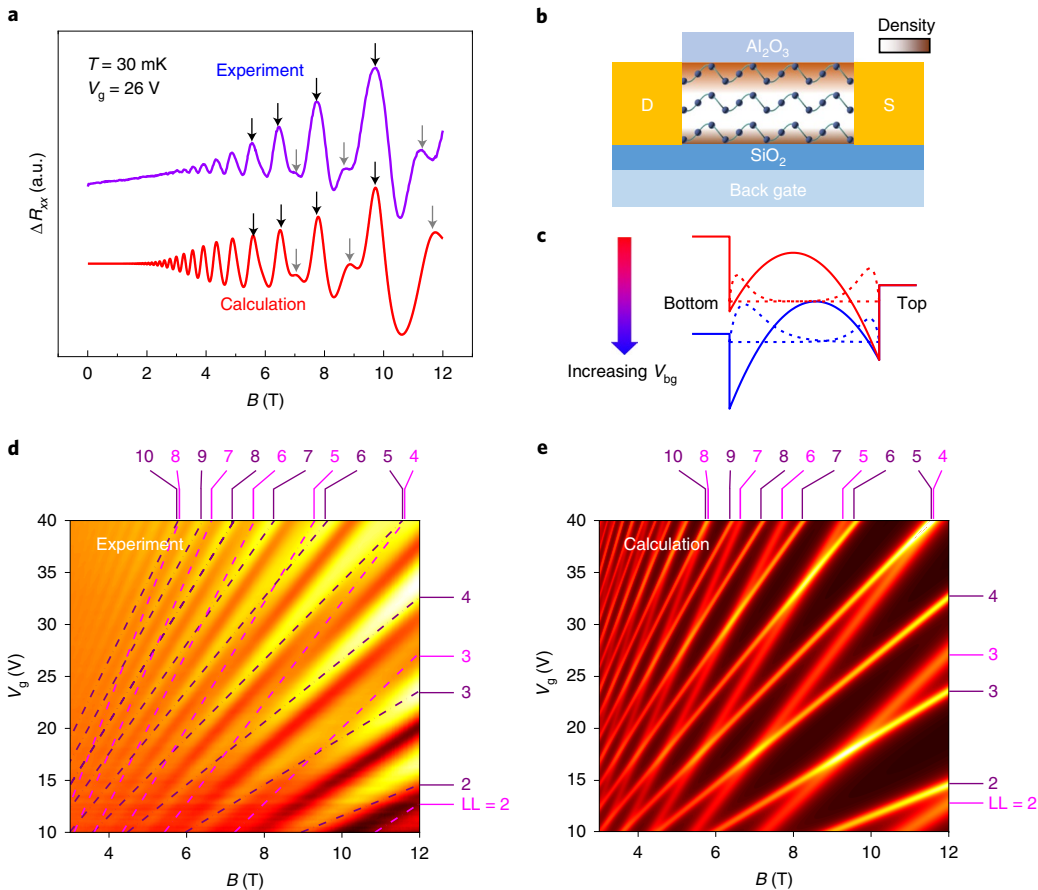


Fig. 3 | Shubnikov-de Haas oscillation analysis of two layers of electrons in a Te wide quantum well. **a**, Representative SdH oscillation features measured at 30 mK and $V_g = 26 \text{ V}$ (top curve) and fitting results (bottom curve) from complete L-K formula with the superposition of two sets of independent oscillations. The black arrows mark the predominant set (bottom layer) and the grey arrows represent the weaker set (top layer). **b**, Schematics of a back-gate device and carrier distribution on top and bottom of the Te film. **c**, Potential profile and wave function distribution of two layers of charge with increasing back gate voltage (from red to blue). **d**, **e**, Experimental (**d**) and simulation (**e**) of R_{xx} mapping in B - V_{bg} parameter space. The purple and light magenta dashed lines and labels on the side indicate Landau level (LL) index of back and top layers of electrons. The dashed lines are plotted by integer fraction of B_L .

we fix the phase offset φ_D at π , not 0. Furthermore, the purple and magenta dashed lines in Fig. 3d plotted from $B_n = B_f(V_g)/n$ (where $B_f(V_g)$ is the oscillation frequency under gate bias V_g and n is a positive integer) coincide with the bright strips which represent maxima in the oscillations. This instantly distinguishes Te from other trivial semiconductor systems. The Onsager-Lifshitz quantization rule dictates the oscillation amplitude to take the form

$$\Delta R_{xx} \propto \cos(2\pi(B_F/B + 1/2) + \varphi) \quad (3)$$

and thus in a trivial semiconductor system where $\varphi = 0$, the n -th Landau level should be observed at field $B_n = B_f(V_g)/(n + \frac{1}{2})$. This suggests that the SdH oscillations in the Te system possess a phase offset $\varphi = \pi$, originating from the contribution of the π Berry phase near the Weyl node, as we shall discuss next.

Evidence of Weyl fermions existing in bulk Te has been reported, such as observations of negative magnetoresistance³⁹ and the kinetic magnetoelectric¹⁰ effect. Here, we present much more convincing evidence that the π Berry phase is involved in quantum oscillations. As a common practice, the phase offset is read off from the intercept of the Landau fan diagram. To construct the Landau fan diagram correctly, the resistivity ρ_{xx} and ρ_{xy} was first properly converted into conductivity σ_{xx} and σ_{xy} with an anisotropic Hall tensor (see Supplementary Note 2) to avoid phase shift⁴⁰, since the fundamental

quantization occurs in conductivity and not resistivity^{41,42}. The minima in conductivity σ_{xx} are assigned with integer index n and the maxima are identified with half integers and then plotted against $1/B$. As shown in Fig. 4a,b, the extrapolated linear fitting curves intercept the y axis at $1/2$ throughout the entire gate range, which was also observed in many other Dirac or Weyl topological materials with a non-trivial π Berry phase^{2,3,43–45}. We shall point out that it can be risky to associate directly a phenomenological phase offset in oscillations with the Berry phase of Dirac/Weyl fermions in some scenarios^{46,47} due to orbital moments and/or Zeeman effects. However, in a spin-orbit coupled system with time reversal symmetry but not spatial inversion symmetry like Te, the phase contributions from orbital moment and Zeeman effect cancel out due to symmetry. Therefore, it is safe to take the π phase offset as a smoking gun for Weyl fermions in this case⁴⁸. We can rule out another trivial cause of π phase offset due to large Zeeman splitting (like in the case of WSe₂, see ref. ⁴⁹) by the absence of a coincident effect when rotating the sample (see Supplementary Note 3 and Extended Data Fig. 2). Furthermore, to eliminate assertively any potential offset from imperfection of the device, we measured another eight devices and all of them unanimously show near π phase shift in SdH oscillation features (see Supplementary Note 4 and Extended Data Fig. 3).

The origin of the Berry phase is rooted in the hedgehog-like spin texture^{6,9} near the chirality-induced Weyl nodes. A weak

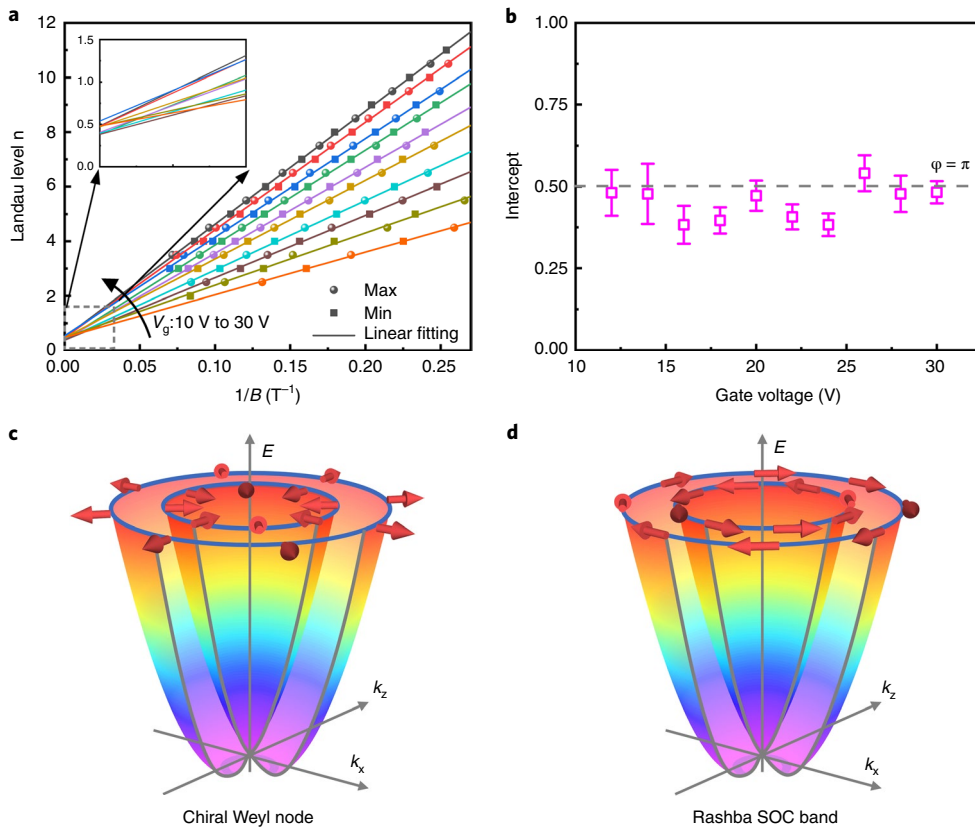


Fig. 4 | Weyl nodes and Berry phase near Te conduction band edge. **a**, Landau fan diagram under different gate bias. The scattered symbols are read off from the value $1/B$ of minima in σ_{xx} and plotted against the Landau level index. Straight lines are linear fitting under each gate bias. Inset: Magnified view of grey dashed box in **a** with linear fittings extrapolated to the y axis. **b**, Intercept of linear fittings versus gate voltage. Error bars represent s.d. from linear fitting. The reference line at $y=0.5$ corresponds to the π Berry phase. **c**, The energy dispersion E and spin texture (red arrows) in a chirality-induced Weyl node at the H point in two-dimensional momentum space k_x - k_z . **d**, A conventional Rashba SOC band.

anti-localization effect is observed in the near-zero magnetic field regime (see Supplementary Note 5), indicating strong SOC in Te (ref. ⁵⁰). The strong SOC gives rise to a spin-polarized band crossing at the H and H' points (as shown in Fig. 4c), which is protected by the three-fold rotational symmetry. This point at H (and also the point at H') is classified as a Weyl node^{6–9} that can be viewed as a Berry curvature monopole in the momentum space⁸. The spin textures are either pointing at or away from the Weyl nodes as illustrated by red arrows in Fig. 4c, which is in sharp contrast to a conventional Rashba SOC band whose energy dispersion may be similar, but whose spin texture is tangential (Fig. 4d). Under magnetic fields when an electron completes a cyclotron motion in the real space its momentum changes by 2π , corresponding to a closed orbit around the Fermi surface in momentum space. Along this path, the spin of the electron also rotates by 2π , which picks up a π Berry phase, since electrons are spin 1/2 particles. The hedgehog-like spin texture near Te Weyl nodes resembles that near the Dirac points of graphene which also give rise to a topologically non-trivial π Berry phase, except that in graphene the Berry phase is induced by a radial pseudospin (valley isospin) texture^{51,52} rather than the real spin as in Te.

We note that, unlike normal band-inversion-induced Weyl semimetals which usually lead to linear band dispersion in a broader energy window, chirality-induced Weyl nodes can potentially exist near the band edge of a semiconductor system. These semiconductor systems with chirality-induced Weyl nodes grant us extended tunability to probe the topological properties of Weyl fermions by taking advantage of the versatility of semiconductors.

A sharp contrast between Te and other Weyl semimetals is seen in the effective mass measurement. In a nutshell, the Weyl nodes only guarantee the topological properties, but the band dispersion can still be arbitrary, depending on the energy scale of interest. For example, band-inversion-induced Dirac nodes in graphene are accompanied by linear band dispersion for the entire gate-accessible range near the Dirac points, since the first order of Hamiltonian can be accurately described by the Dirac equation in the energy window near 1 eV. This gives rise to a strongly gate-dependent cyclotron mass of relativistic Dirac fermions: $m_c = \frac{E_F}{v_F} = \sqrt{\pi\hbar^2 n_s/v_F^2}$ (here m_c is cyclotron mass, E_F is Fermi energy, v_F is Fermi velocity and n_s is sheet density, respectively), as confirmed by temperature-dependent SdH oscillation amplitudes⁵³. Here, we also extract the cyclotron mass by fitting the temperature-dependent SdH amplitude with the thermal damping term in the L-K formula (Fig. 5a)

$$\Delta R_{xx} \propto \frac{2\pi^2 m^* k_B T / \hbar e B}{\sinh(2\pi^2 m^* k_B T / \hbar e B)} \quad (4)$$

The cyclotron mass is extracted to be $0.097 \pm 0.008 m_0$ (where m_0 is the free electron mass) regardless of the gate bias (Fig. 5b), which is consistent with the previously reported value for bulk Te^{53,54}. This is because chirality-induced Weyl nodes reside only several meV above the conduction band minima and the semiconductor properties (for example band mass) are preserved. Meanwhile, the topological properties (Berry phase) carry over to a much broader energy window of at least 50 meV that the gate can access.

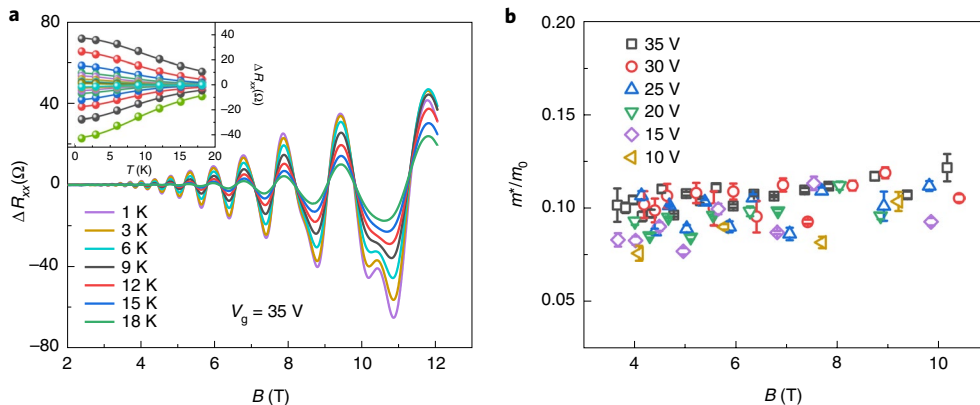


Fig. 5 | Temperature-dependent SdH oscillations and effective mass of Weyl fermions. **a**, SdH oscillation amplitudes (subtracting a smooth background) under various temperature from 0.5 K to 18 K. Inset: ΔR_{xx} versus temperature fitted by thermal damping term of L-K formula. **b**, The effective mass (m^*) is extracted to be about $0.097 \pm 0.008 m_0$ (where m_0 is the bare electron mass) and is independent of gate biases and magnetic fields. Error bars represent standard error from L-K formula fitting.

Conclusions

In conclusion, using ALD dielectric doping on high-quality tellurene films, for the first time we observed a well-developed quantum Hall effect of a 2D electron gas in tellurene and accessed the electronic structure of its conduction band. A wide quantum-well model with two layers of electrons is proposed to explain the anomaly in SdH oscillations and quantum Hall sequences. Spin and valley isospin degeneracies are fully lifted under 45 T external magnetic field, leading to fully polarized quantum Hall ferromagnetic states. The topologically non-trivial π Berry phase is unambiguously detected and serves as direct evidence of Weyl fermions in the vicinity of chirality-induced Weyl nodes with predicted hedgehog-like spin textures. Therefore, n-type Te is an ideal material to explore the topological properties of relativistic quasiparticles in a chiral semiconductor system with tunable Fermi surface and exploitable band gap.

Online content

Any methods, additional references, Nature Research reporting summaries, source data, extended data, supplementary information, acknowledgements, peer review information; details of author contributions and competing interests; and statements of data and code availability are available at <https://doi.org/10.1038/s41565-020-0715-4>.

Received: 29 January 2020; Accepted: 12 May 2020;

Published online: 29 June 2020

References

- Geim, A. K. & Novoselov, K. S. The rise of graphene. *Nat. Mater.* **6**, 183–191 (2007).
- Novoselov, K. S. et al. Two-dimensional gas of massless Dirac fermions in graphene. *Nature* **438**, 197–200 (2005).
- Zhang, Y. B., Tan, Y. W., Stormer, H. L. & Kim, P. Experimental observation of the quantum Hall effect and Berry's phase in graphene. *Nature* **438**, 201–204 (2005).
- Armitage, N. P., Mele, E. J. & Vishwanath, A. Weyl and Dirac semimetals in three-dimensional solids. *Rev. Mod. Phys.* **90**, 015001 (2018).
- Hasan, M. Z., Xu, S. Y., Belopolski, I. & Huang, S. M. Discovery of Weyl fermion semimetals and topological Fermi arc states. *Annu. Rev. Condens. Matter Phys.* **8**, 289–309 (2017).
- Hirayama, M., Okugawa, R., Ishibashi, S., Murakami, S. & Miyake, T. Weyl node and spin texture in trigonal tellurium and selenium. *Phys. Rev. Lett.* **114**, 206401 (2015).
- Nakayama, K. et al. Band splitting and Weyl nodes in trigonal tellurium studied by angle-resolved photoemission spectroscopy and density functional theory. *Phys. Rev. B* **95**, 125204 (2017).
- Tsirkin, S. S., Puente, P. A. & Souza, I. Gyrotropic effects in trigonal tellurium studied from first principles. *Phys. Rev. B* **97**, 035158 (2018).
- Agapito, L. A., Kioussis, N., Goddard, W. A. & Ong, N. P. Novel family of chiral-based topological insulators: elemental tellurium under strain. *Phys. Rev. Lett.* **110**, 176401 (2013).
- Şahin, C., Rou, J., Ma, J. & Pesin, D. A. Pancharatnam-Berry phase and kinetic magnetoelectric effect in trigonal tellurium. *Phys. Rev. B* **97**, 205206 (2018).
- Chang, G. et al. Topological quantum properties of chiral crystals. *Nat. Mater.* **17**, 978 (2018).
- Rao, Z. et al. Observation of unconventional chiral fermions with long Fermi arcs in CoSi. *Nature* **567**, 496–499 (2019).
- Sanchez, D. S. et al. Topological chiral crystals with helicoid-arc quantum states. *Nature* **567**, 500–505 (2019).
- Zhang, C. L. et al. Ultraquantum magnetoresistance in the Kramers–Weyl semimetal candidate β -Ag₃Se. *Phys. Rev. B* **96**, 1–10 (2017).
- von Klitzing, K. & Landwehr, G. Surface quantum states in tellurium. *Solid State Commun.* **9**, 2201–2205 (1971).
- Silbermann, R. & Landwehr, G. Surface quantum oscillations in accumulation and inversion layers on tellurium. *Solid State Commun.* **16**, 6–9 (1975).
- von Klitzing, K. Magnetophon oscillations in tellurium under hot carrier conditions. *Solid State Commun.* **15**, 1721–1725 (1974).
- Wang, Y. et al. Field-effect transistors made from solution-grown two-dimensional tellurene. *Nat. Electron.* **1**, 228–236 (2018).
- Du, Y. et al. One-dimensional van der Waals material tellurium: Raman spectroscopy under strain and magneto-transport. *Nano Lett.* **17**, 3965–3973 (2017).
- Wu, W., Qiu, G., Wang, Y., Wang, R. & Ye, P. Tellurene: its physical properties, scalable nanomanufacturing, and device applications. *Chem. Soc. Rev.* **47**, 7203–7212 (2018).
- Qiu, G. et al. Quantum transport and band structure evolution under high magnetic field in few-layer tellurene. *Nano Lett.* **18**, 5760–5767 (2018).
- Gusynin, V. P. & Sharapov, S. G. Unconventional integer quantum Hall effect in graphene. *Phys. Rev. Lett.* **95**, 146801 (2005).
- Li, L. et al. Quantum oscillations in a two-dimensional electron gas in black phosphorus thin films. *Nat. Nanotechnol.* **10**, 608–613 (2015).
- Li, L. et al. Quantum hall effect in black phosphorus two-dimensional electron system. *Nat. Nanotechnol.* **11**, 593–597 (2016).
- Yang, J. et al. Integer and fractional quantum Hall effect in ultra-high quality few-layer black phosphorus transistors. *Nano Lett.* **18**, 229–234 (2018).
- Bandurin, D. A. et al. High electron mobility, quantum Hall effect and anomalous optical response in atomically thin InSe. *Nat. Nanotechnol.* **12**, 223–227 (2017).
- Fallahazad, B. et al. Shubnikov-de Haas oscillations of high-mobility holes in monolayer and bilayer WSe₂: Landau level degeneracy, effective mass, and negative compressibility. *Phys. Rev. Lett.* **116**, 1–5 (2016).
- Movva, H. C. P. et al. Density-dependent quantum Hall states and Zeeman splitting in monolayer and bilayer WSe₂. *Phys. Rev. Lett.* **118**, 247701 (2017).
- Wu, Z. et al. Even-odd layer-dependent magnetotransport of high-mobility Q-valley electrons in transition metal disulfides. *Nat. Commun.* **7**, 12955 (2016).
- Pisoni, R. et al. Interactions and magnetotransport through spin-valley coupled Landau levels in monolayer MoS₂. *Phys. Rev. Lett.* **121**, 247701 (2018).

31. Ren, X. et al. Gate-tuned insulator-metal transition in electrolyte-gated transistors based on tellurene. *Nano Lett.* **19**, 4738–4744 (2019).
32. Qiu, G. et al. High-performance few-layer tellurium CMOS devices enabled by atomic layer deposited dielectric doping technique. In *2018 76th Device Research Conference (DRC)* 1–2 (IEEE, 2018).
33. Berweger, S. et al. Imaging carrier inhomogeneities in ambipolar tellurene field effect transistors. *Nano Lett.* **19**, 1289–1294 (2019).
34. Liu, H., Neal, A. T., Si, M., Du, Y. & Ye, P. D. The effect of dielectric capping on few-layer phosphorene transistors: Tuning the Schottky barrier heights. *IEEE Electron Device Lett.* **35**, 795–797 (2014).
35. Perello, D. J., Chae, S. H., Song, S. & Lee, Y. H. High-performance n-type black phosphorus transistors with type control via thickness and contact-metal engineering. *Nat. Commun.* **6**, 7809 (2015).
36. Wang, C. H. et al. Unipolar n-type black phosphorus transistors with low work function contacts. *Nano Lett.* **18**, 2822–2827 (2018).
37. Coss, B. E. et al. Near band edge Schottky barrier height modulation using high- κ dielectric dipole tuning mechanism. *Appl. Phys. Lett.* **95**, 222105 (2009).
38. Klitzing, K. V., Dorda, G. & Pepper, M. New method for high-accuracy determination of the fine-structure constant based on quantized Hall resistance. *Phys. Rev. Lett.* **45**, 494–497 (1980).
39. Zhang, N. et al. Evidence for Weyl fermions in the elemental semiconductor tellurium. *arXiv Prepr. arXiv1906.06071* (2019).
40. Ren, Z., Taskin, A. A., Sasaki, S., Segawa, K. & Ando, Y. Large bulk resistivity and surface quantum oscillations in the topological insulator Bi₂Te₂Se. *Phys. Rev. B* **82**, 241306 (2010).
41. Ando, Y. Topological insulator materials. *J. Phys. Soc. Jpn.* **82**, 102001 (2013).
42. Xiong, J. et al. Quantum oscillations in a topological insulator Bi₂Te₂Se with large bulk resistivity (6Ω•cm). *Phys. E* **44**, 917–920 (2012).
43. Yu, W. et al. Quantum oscillations at integer and fractional Landau level indices in single-crystalline ZrTe₅. *Sci. Rep.* **6**, 35357 (2016).
44. Hu, J. et al. π Berry phase and Zeeman splitting of Weyl semimetal TaP. *Sci. Rep.* **6**, 18674 (2016).
45. Zhao, Y. et al. Anisotropic Fermi surface and quantum limit transport in high mobility three-dimensional dirac semimetal Cd₃As₂. *Phys. Rev. X* **5**, 031037 (2015).
46. Roth, L. Semiclassical theory of magnetic energy levels and magnetic susceptibility of Bloch electrons. *Phys. Rev.* **145**, 434 (1966).
47. Dhillon, J. S. & Shoenberg, D. The de Haas-van alphen effect III. Experiments at fields up to 32 KG. *Philos. Trans. R. Soc. A* **248**, 1–21 (1955).
48. Alexandradinata, A., Wang, C., Duan, W. & Glazman, L. Revealing the topology of Fermi-surface wave functions from magnetic quantum oscillations. *Phys. Rev. X* **8**, 11027 (2018).
49. Xu, S. et al. Odd-integer quantum hall states and giant spin susceptibility in p-type few-layer WSe₂. *Phys. Rev. Lett.* **118**, 067702 (2017).
50. Niu, C. et al. Gate-tunable Strong Spin-orbit Interaction in Two-dimensional Tellurium Probed by Weak-antilocalization. *arXiv Prepr. arXiv1909.06659* (2019).
51. Rotenberg, E. Topological insulators: The dirt on topology. *Nat. Phys.* **7**, 8–10 (2011).
52. Mallet, P. et al. Role of pseudospin in quasiparticle interferences in epitaxial graphene probed by high-resolution scanning tunneling microscopy. *Phys. Rev. B* **86**, 045444 (2012).
53. Shinno, H., Yoshizaki, R., Tanaka, S., Doi, T. & Kamimura, H. Conduction band structure of tellurium. *J. Phys. Soc. Jpn.* **35**, 525–533 (1973).
54. Liu, Y., Wu, W. & Goddard, W. A. Tellurium: fast electrical and atomic transport along the weak interaction direction. *J. Am. Chem. Soc.* **140**, 550–553 (2018).

Publisher's note Springer Nature remains neutral with regard to jurisdictional claims in published maps and institutional affiliations.

© The Author(s), under exclusive licence to Springer Nature Limited 2020

Methods

Hydrothermal growth of 2D tellurium films. The hydrothermal growth process of Te twin flakes is similar to previously reported methods of growing tellurene nanofilms¹⁸. To start with, Na₂TeO₃ (0.104 g) and polyvinylpyrrolidone (0.5479 g) (Sigma-Aldrich) were put into a 50 ml teflon-lined stainless steel autoclave and dissolved in 33 ml of double-distilled water under vigorous magnetic stirring to form a homogeneous solution at room temperature. Aqueous ammonia solution (3.648 ml, 25–28%, w/w%) and hydrazine hydrate (1.824 ml, 85%, w/w%) were added sequentially into the mixed solution under vigorous magnetic stirring. The autoclave was sealed and heated at 180 °C for 23 h and then cooled naturally to room temperature.

Langmuir–Blodgett transfer of 2D Te films. The as-grown 2D Te films were first cleaned twice with de-ionized (DI) water and then dispersed onto arbitrary substrate by the Langmuir–Blodgett technique⁵⁵. The suspension was first centrifuged to remove aqueous solution and remaining ions and then a mixture of solvents *N,N*-dimethylformamide and CHCl₃ (for example, in a ratio of 1.3:1) was added as a dispersant. The mixture was subsequently dropped onto DI water after which the hydrophilic Te films could float on the water surface and were scooped onto heavily doped Si substrates with a 90 nm SiO₂ insulating layer.

Device fabrication. Following a DI water rinse and standard solvent cleaning process (acetone, methanol and isopropanol), Hall-bar devices were patterned using electron beam lithography and 30/90 nm Ti/Au metal contacts were deposited by electron beam evaporation at a pressure below 2 × 10⁻⁶ Torr. To eliminate geometric non-idealities, the device was then trimmed into a standard Hall bar shape with better symmetry using BC_l/Ar dry etching. Al₂O₃ (20 nm) was deposited onto the Te films at 200 °C with ALD to achieve n-type doping.

Magneto-transport measurements. Low magnetic field transport measurements were performed using a Triton 300 (Oxford Instruments) dilution fridge system with 12 T superconducting coils. The high magnetic field data were acquired in a 31 T resistive magnet system (Cell 9) and a 45 T hybrid magnet system (Cell 15) at the National High Magnetic Field Laboratory (NHMFL) in Tallahassee, FL. Electrical data was recorded using standard low frequency AC measurement techniques with SR830 lock-in amplifiers. The transfer curves of two-terminal FETs were measured with a Cascade probe station and Keysight B1500A semiconductor analyser at room temperature and using the current mode of a lock-in amplifier at 30 mK.

Data availability

The data that supports the argument and generates the plots in this paper are available from the corresponding author upon reasonable request.

References

55. Zasadzinski, J. A., Viswanathan, R., Madsen, L., Garnaes, J. & Schwartz, D. K. Langmuir–Blodgett films. *Science* **263**, 1726–1733 (1994).

Acknowledgements

P.D.Y. was supported by NSF/AFOSR 2DARE programmes ARO and SRC. W.W. acknowledges the College of Engineering and School of Industrial Engineering at Purdue University for the startup support. W.W. was partially supported by a grant from the Oak Ridge Associated Universities (ORAU) Junior Faculty Enhancement Award Programme. W.W. and P.D.Y. were also supported by NSF under grant no. CMMI-1762698. A portion of this work was performed at the National High Magnetic Field Laboratory, which is supported by National Science Foundation Cooperative Agreement No. DMR-1644779 and the State of Florida. G.Q. and C.N. acknowledge technical support from National High Magnetic Field Laboratory staff J. Jaroszynski, A. Suslov and W. Coniglio. The authors want to give special thanks to K. von Klitzing, T. Ando, W. Pan, K. Chang, F. Zhang, C. Liu, K. Cho, Y. Nie and J. Hwang for the insightful discussions on electronic structures of Te. The authors also acknowledge A. R. Charnas for editorial assistance.

Author contributions

P.D.Y. conceived and supervised the project. P.D.Y. and G.Q. designed the experiments. Y.W. synthesized the material under the supervision of W.W. G.Q. and C.N. fabricated the devices. G.Q., C.N. and Z.Z. performed the magneto-transport measurements. G.Q., C.N., M.S. and Z.Z. analysed the data. P.D.Y. and G.Q. wrote the manuscript with input and comments from all the authors.

Competing interests

The authors declare no competing interests.

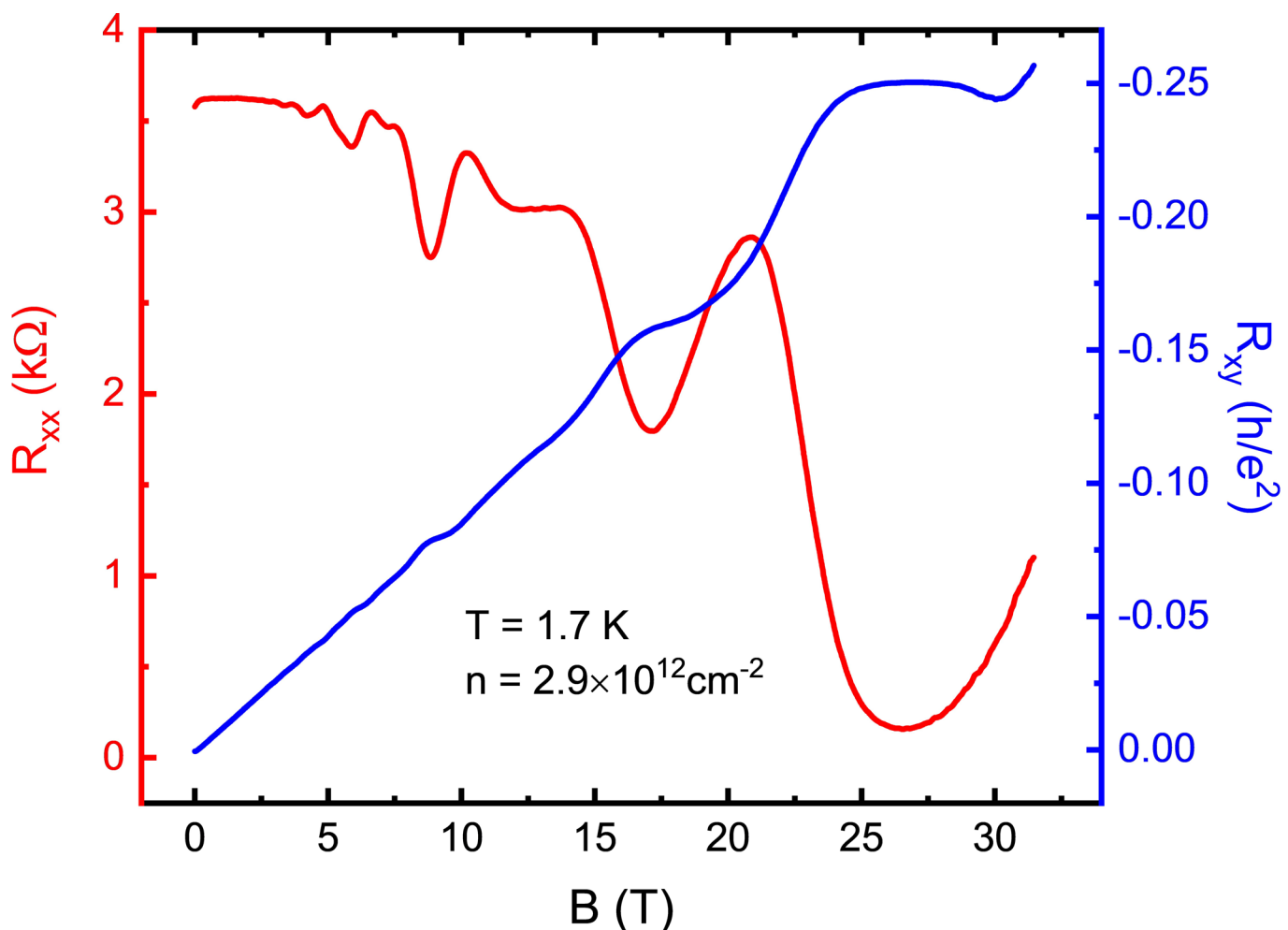
Additional information

Extended data is available for this paper at <https://doi.org/10.1038/s41565-020-0715-4>.

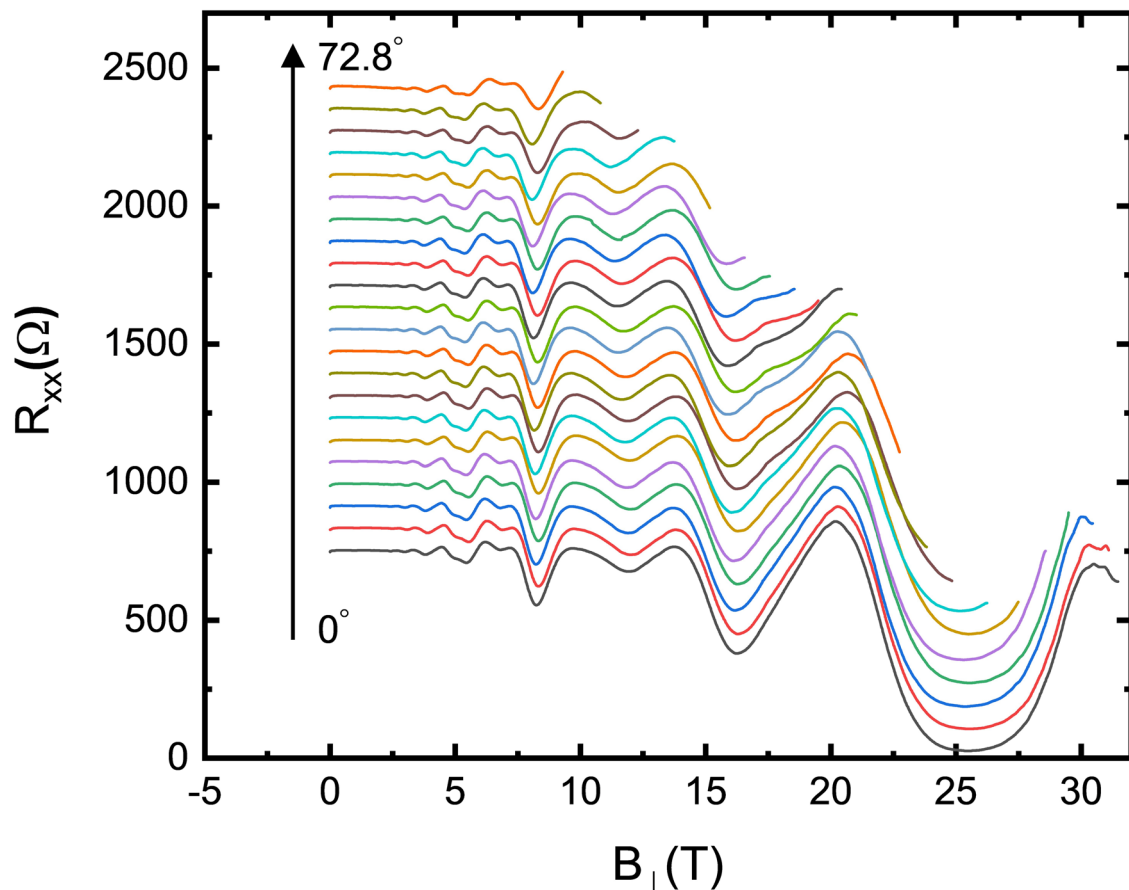
Supplementary information is available for this paper at <https://doi.org/10.1038/s41565-020-0715-4>.

Correspondence and requests for materials should be addressed to P.D.Y.

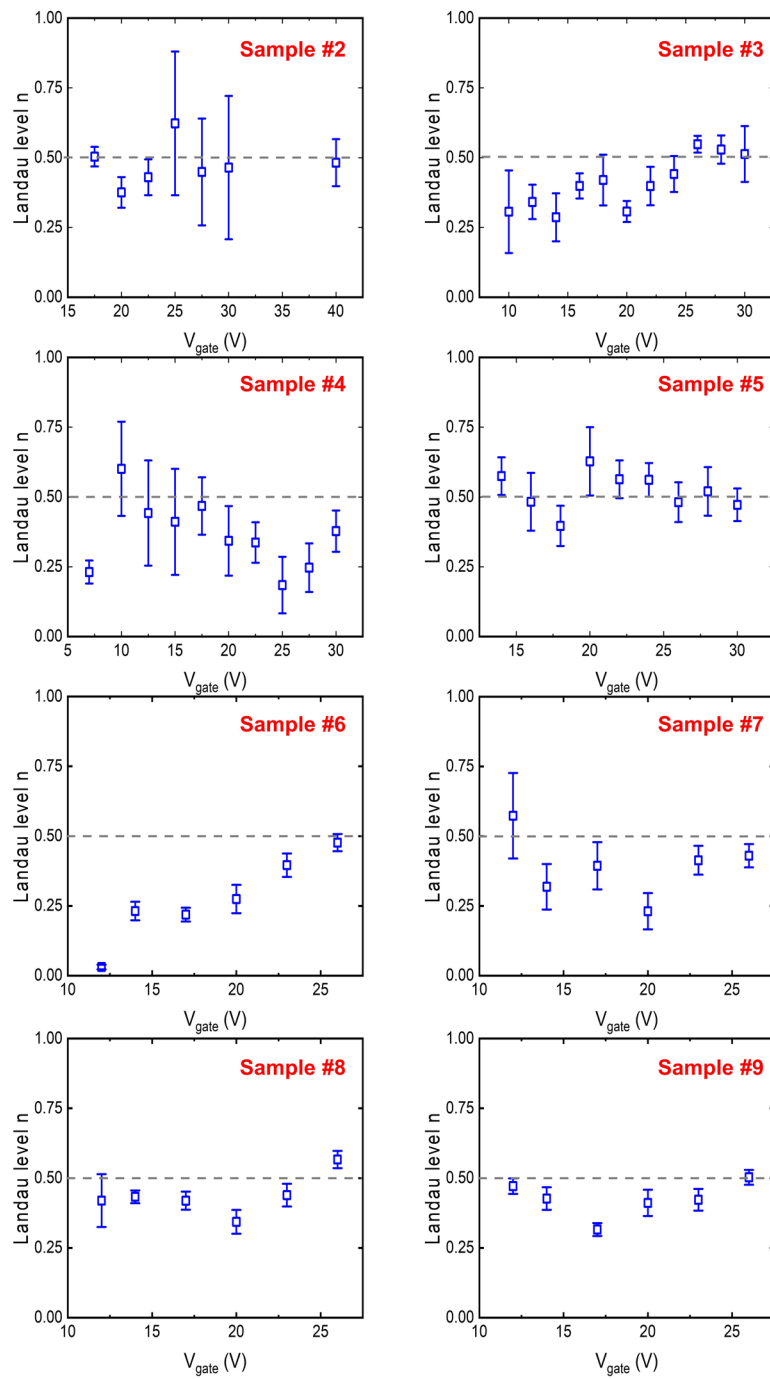
Reprints and permissions information is available at www.nature.com/reprints.



Extended Data Fig. 1 | Quantum Hall effect of another high mobility sample. Longitudinal (R_{xx} , red) and transverse (R_{xy} , blue) resistance measured under magnetic field up to 31.4 T at 1.7 K.



Extended Data Fig. 2 | SdH oscillations in a tilted magnetic field. The curves are separated by 80 Ω offset for clarity. No evidence of coincidence effect is observed, suggesting a small effective g -factor.



Extended Data Fig. 3 | Extracting Berry phase using SdH oscillation phase offset from eight more devices.